Available online at website: https://journal.bcrec.id/index.php/bcrec

Bulletin of Chemical Reaction Engineering & Catalysis, 22 (1) 2027, 13-24

Original Research Article

The Effect of Sintering Temperature on the Structural Characteristics, Particle Size, and Photocatalytic Properties of $BaTiO_3$ and $Ba_{0.97}Sr_{0.03}TiO_3$ Nanomaterials

Elvinda Bendra Agustina[1*], Abdul Hakim Prima Yuniarto[1,3], Alif Tiana Dewi[1], Yofentina Iriani[2], Trya Andini[2]

[1]Department of Physics, Faculty of Science and Technology, Institute of Technology and Science Nahdlatul Ulama Pekalongan, Pekalongan 51173, Indonesia.
[2]Department of Physics, Faculty of Mathematics and Natural Science, Sebelas Maret University, Surakarta 57126, Indonesia.
[3]Department of Electrical Engineering, Sekolah Tinggi Teknik Wiworotomo, Purwokerto, Indonesia.

Received: 7th September 2026; Revised: 22nd October 2026; Accepted: 23rd October 2026
Available online: 30th October 2026; Published regularly: April 2027

Abstract

$BaTiO_3$ and $Ba_{0.97}Sr_{0.03}TiO_3$ nanomaterials were synthesized by the co-precipitation method and sintered at 900 °C and 1000 °C for 4 hours. This study investigates the effect of 3 mol% Sr substitution and sintering temperature on the crystal structure, functional groups, particle-size distribution, and photocatalytic performance toward methylene blue (MB) degradation. X-ray diffraction (XRD) showed tetragonal perovskite $BaTiO_3$ with weak secondary reflections, more numerous in the Sr-containing samples, and no resolved shift of the (101) reflection after Sr substitution. The crystallite size estimated from XRD was 30-33 nm (Scherrer plot) and 37-46 nm (unsplit (111) reflection), whereas dynamic light scattering (DLS) gave Z-average hydrodynamic diameters of about 250-440 nm, indicating agglomeration of the crystallites; the Sr-containing powder was smaller only at 900 °C. FTIR spectra showed the characteristic Ti-O (Ba-Ti-O) stretching band at 565-576 cm^{-1}. Photocatalytic activity was evaluated using 10 ppm MB solution under UV irradiation. The apparent MB removal, calculated from the absorbance at 664 nm, was ≈34% and ≈24% for $Ba_{0.97}Sr_{0.03}TiO_3$ sintered at 900 °C and 1000 °C, compared with ≈28% and ≈0% for undoped $BaTiO_3$; thus Sr substitution increased, and the higher sintering temperature decreased, the apparent removal. The origin of this behavior was not directly characterized and requires further study.

Copyright © 2027 by Authors, Published by BCREC Publishing Group. This is an open access article under the CC BY-SA License (https://creativecommons.org/licenses/by-sa/4.0).

Keywords: Barium titanate; Strontium doping; Co-precipitation; Sintering temperature; Photocatalyst; Methylene blue

How to Cite: Agustina, E. B., Yuniarto, A. H. P., Dewi, A. T., Iriani, Y., Andini, T. (2027). The Effect of Sintering Temperature on the Structural Characteristics, Particle Size, and Photocatalytic Properties of $BaTiO_3$ and $Ba_{0.97}Sr_{0.03}TiO_3$ Nanomaterials. *Bulletin of Chemical Reaction Engineering & Catalysis*, 22 (1), 13-24. (DOI: 10.9767/bcrec.20841)

Permalink/DOI: https://doi.org/10.9767/bcrec.20841

1. Introduction

Industrial activities are important for national development, but they also cause environmental problems [1,2]. Production processes generate large amounts of waste that affect the environment and human health [3,4]. Therefore, the degradation and treatment of organic and inorganic pollutants is a major problem that must be addressed collectively [5,6]. The molecular structures of these pollutants are complex and changeable, which makes them more difficult to decompose than simple molecular pollutants [7]. Advanced oxidation processes (AOPs) utilize free radicals to break down pollutants and are effective for waste treatment [8,9]. Photocatalysis is one of the effective AOPs [10]. A photocatalyst absorbs photons and generates electron-hole pairs (e^- + h^+) that drive reduction and oxidation reactions [11]. Several

* Corresponding Author.
Email: elvindabendra89@gmail.com (E.B. Agustina)

semiconductors have been tested as photocatalysts for pollutant removal, but it is still difficult to find a stable and efficient photocatalyst. Much research has therefore focused on nanostructure engineering, band-gap tuning, and doping to improve photocatalytic efficiency [12-14]. Perovskite-structured semiconductors, such as $SrTiO_3$, $BaTiO_3$, $LaAlO_3$, $BaCeO_3$, and $BaZrO_3$, have been widely studied for various applications. Among them, barium titanate ($BaTiO_3$, BTO) and strontium titanate ($SrTiO_3$, STO) are popular ferroelectric perovskite oxides with potential for photocatalytic applications [15-17]. Sr^{2+}-substituted $BaTiO_3$ has been proposed as a promising photocatalytic material because of its low cost, tunable band gap, and potential response in the visible-light region [18,19]. The ionic radius of Sr^{2+} (1.44 Å) is close to that of Ba^{2+} (1.61 Å), so $BaTiO_3$ can form a continuous solid solution with Sr^{2+}. Barium strontium titanate, $Ba_{1-x}Sr_xTiO_3$ (BST), has a relatively high permittivity and low dielectric leakage, which gives it a good response to externally applied electric fields.

The properties of BST depend strongly on the synthesis route and the thermal treatment. Hikmah *et al.* [20] prepared $SrTiO_3$ by co-precipitation and sintered it at 800 °C and 900 °C for 2 and 4 hours; the sintering temperature and holding time changed the intensity and width of the XRD peaks and, consequently, the crystallite size and lattice strain. Ali *et al.* [21] synthesized $Ba_{1-x}Sr_xTi_4O_9$ ($0.0 \leq x \leq 0.06$) by solid-state reaction at 1300 °C for 2 hours and reported that a higher Sr^{2+} content increased the dielectric constant (ε_r) and the dielectric loss (tan δ). BST has also been prepared by the sol-gel method [22], solid-state reaction [23], chemical solution deposition [24], and co-precipitation [25]. In this research, co-precipitation was chosen because it produces powders with good homogeneity, allows easy control of stoichiometry, and yields ferroelectric nanomaterials at relatively low sintering temperatures and short processing times through a simple and low-risk procedure [26].

The studies cited above mainly addressed the structural, dielectric, or optical properties of Sr-containing titanates, and the thermal treatment was usually discussed independently of photocatalytic performance (Table 1). To the best of our knowledge, reports that combine a small Sr content (3 mol%) with a systematic variation of the sintering temperature for co-precipitated $BaTiO_3$, and that compare structural parameters with the photocatalytic response of the same powders, remain limited. This combination is relevant because sintering temperature simultaneously affects crystallinity, crystallite size, secondary-phase content, and agglomeration, all of which may influence photocatalytic activity.

Therefore, this study synthesizes $BaTiO_3$ and $Ba_{0.97}Sr_{0.03}TiO_3$ by co-precipitation, sinters them at 900 °C and 1000 °C, and analyzes their crystal structure, functional groups, particle-size distribution, and photocatalytic activity toward MB under UV irradiation, in order to clarify how a small Sr content and the sintering temperature affect these properties.

2. Materials and Methods

2.1. Materials and Synthesis Procedure

$BaTiO_3$ and $Ba_{0.97}Sr_{0.03}TiO_3$ were synthesized by the co-precipitation method using barium hydroxide [$Ba(OH)_2$] (Sigma-Aldrich, 95%), titanium tetrabutoxide [$Ti(C_4H_9O)_4$] (Sigma-Aldrich, 97%), oxalic acid dihydrate ($H_2C_2O_4 \cdot 2H_2O$) (Sigma-Aldrich, ≥ 99%), strontium nitrate [$Sr(NO_3)_2$], isopropanol (IPA), ethanol, and distilled water. The target molar ratios were Ba:Sr:Ti = 1:0:1 for $BaTiO_3$ and 0.97:0.03:1 for $Ba_{0.97}Sr_{0.03}TiO_3$. The amounts used per batch (0.00999 mol Ti) were: $Ti(C_4H_9O)_4$ 3.4 mL; $Ba(OH)_2$ 1.7100 g for $BaTiO_3$ and 1.6604 g for $Ba_{0.97}Sr_{0.03}TiO_3$; $Sr(NO_3)_2$ 0.0634 g ($Ba_{0.97}Sr_{0.03}TiO_3$ only); and oxalic acid dihydrate 3.5304 g (oxalic acid : Ti molar ratio ≈ 2.8:1).

Table 1. Comparison of the present work with previous studies on Sr-containing and related titanates.

Material	Synthesis and thermal treatment	Main properties studied	Ref.
$SrTiO_3$	Co-precipitation; 800 and 900 °C, 2 and 4 h	Crystallite size, lattice strain, chemical bonds	[20]
$Ba_{1-x}Sr_xTi_4O_9$ ($0.0 \leq x \leq 0.06$)	Solid-state reaction; 1300 °C, 2 h	Structure, dielectric constant and loss	[21]
$Ba_{0.95}Sr_{0.05}TiO_3$ films	Chemical solution deposition; annealing temperature varied	Microstructure, optical properties	[24]
$Ba_{1-x}La_xTiO_3$	Co-precipitation; La content varied	Microstructure, morphology, dielectric properties	[25]
$BaTiO_3$ and $Ba_{0.97}Sr_{0.03}TiO_3$	Co-precipitation; 900 and 1000 °C, 4 h	Crystal structure, bonding, particle size, MB photodegradation	This work

Copyright © 2027, ISSN 1978-2993

The synthesis steps are summarized in Figure 1. The precursors were first weighed according to the stoichiometric composition. Oxalic acid dihydrate was dissolved in 35 mL of IPA and stirred at 250 rpm for 20 minutes using a magnetic stirrer on a hot plate. Separately, $Ba(OH)_2$ (and $Sr(NO_3)_2$ for the Sr-containing sample) was dissolved in 20 mL of IPA and stirred for 30 minutes. Titanium tetrabutoxide was then added to the oxalic acid solution and stirred at 250 rpm for 20 minutes. The $Ba(OH)_2$ (and $Sr(NO_3)_2$) solution was added gradually to the Ti–oxalic acid solution under continuous stirring, and the mixture was stirred for 30 minutes to obtain a homogeneous suspension. The suspension was aged for 1 hour and then left to precipitate for 24 hours. The pH of the solution was measured after precipitation. The precipitate was separated by filtration (funnel and filter paper) and washed once with ethanol and twice with distilled water, while the pH of the filtrate was monitored. The washed precipitate was dried at 100 °C for 10 hours and ground for 1 hour with the addition of 2-3 drops of polyvinyl alcohol (PVA) as a binder. The powder was sintered in a furnace at 900 °C and 1000 °C for 4 hours to investigate the effect of sintering temperature, and the sintered powder was ground again for 30 minutes before characterization.

2.2. Catalyst Characterizations

The crystal structure of the powders was characterized by XRD (Bruker D8 Advance, Cu Kα radiation, λ = 1.5406 Å, 40 kV, 35 mA, position-sensitive detector) in the 2θ range of 10°-80° with a step size of 0.0237° and a scan time of 10 minutes; the patterns are displayed for 20°-80°. Phases were identified using ICDD card No. 83-1880 for $BaTiO_3$. Lattice parameters of the tetragonal phase were estimated from the positions of the (002) and (200) reflections, obtained by pseudo-Voigt peak fitting. The interplanar spacing d was calculated from the Bragg law:

$$d = \frac{\lambda}{2\sin\theta} \quad (1)$$

and the lattice parameters a and c were obtained from the spacings of the (200) and (002) planes, respectively:

$$a = 2d_{200} \quad (2)$$
$$c = 2d_{002} \quad (3)$$

The crystallite size (D) was obtained with the Scherrer-plot method:

$$\ln\beta = \ln\left(\frac{K\lambda}{D}\right) + \ln\left(\frac{1}{\cos\theta}\right) \quad (4)$$

where β is the full width at half maximum (FWHM, in radians, not corrected for instrumental broadening), K = 0.94 is the shape factor, λ = 0.15406 nm is the X-ray wavelength, and θ is the Bragg angle. The FWHM of ten reflections between 2θ = 22° and 79° were fitted by linear regression, and D was obtained from the intercept b of the fit of ln β versus ln(1/cos θ) (b = ln($K\lambda/D$)):

$$D = \frac{K\lambda}{\exp(b)} \quad (5)$$

For comparison, D was also calculated for the (111) reflection alone:

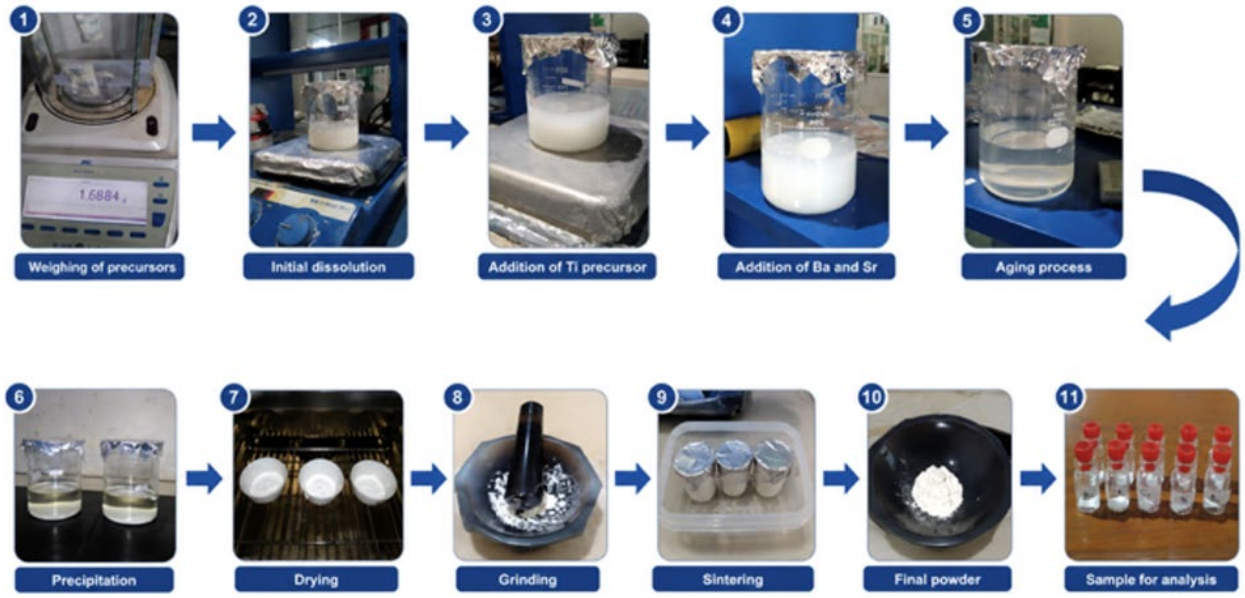


Figure 1. Synthesis procedure of $BaTiO_3$ and $Ba_{0.97}Sr_{0.03}TiO_3$ powders.

Copyright © 2027, ISSN 1978-2993

$$D = \frac{K\lambda}{\beta \cos\theta} \quad (6)$$

Only one measurement per sample was made, so no standard deviation is available. A crystallinity index was calculated as:

$$Crystallinity\ index\ (\%) = \frac{I_{max} - I_{min}}{I_{max}} \times 100 \quad (7)$$

where I_{max} is the intensity of the strongest reflection and I_{min} is the background intensity of the pattern. FTIR spectra were recorded in the range of 350–4000 cm^{-1} using a Shimadzu FTIR spectrophotometer with the KBr pellet method. The particle-size distribution was measured by dynamic light scattering (DLS) using a Malvern Panalytical Zetasizer (software v8.00.4813; measurements on 15 September 2022; three repeated runs per sample). The Z-average hydrodynamic diameter, the polydispersity index (PDI), and the intensity-weighted peak size are reported. PSA provides only the size distribution of particles and agglomerates dispersed in a liquid; therefore, it was not used to evaluate morphology or microstructure.

2.3. Photocatalytic activity test

The photocatalytic activity was evaluated by the degradation of MB under UV irradiation. For each test, 20 mg of $BaTiO_3$ or $Ba_{0.97}Sr_{0.03}TiO_3$ (sintered at 900 °C or 1000 °C) was dispersed in 50 mL of 10 ppm MB solution. The suspension was first stirred in the dark for 30 minutes to reach adsorption-desorption equilibrium. It was then irradiated with a 15 W UV-A lamp at a constant distance of 10 cm above the solution surface, at room temperature, with constant magnetic stirring at 300 rpm to keep the suspension homogeneous. Aliquots were taken every 15 minutes during a total irradiation time of 90 minutes. The catalyst was removed from each aliquot by centrifugation or filtration through a 0.22 μm syringe filter, and the absorbance was measured with a Shimadzu UV-2600i double-beam spectrophotometer (UPT *Laboratorium Terpadu*, Universitas Sebelas Maret) using distilled water as the solvent, at 664 nm, the absorption maximum of MB.

The apparent removal was calculated relative to the absorbance of the untreated 10 ppm MB solution (A_0) measured with the same instrument. No catalyst-free blank (photolysis) data are available. The apparent degradation efficiency was calculated as:

$$\eta(\%) = \frac{C_0 - C_t}{C_0} \times 100 \quad (8)$$

where C_0 and C_t are the MB concentrations of the untreated and the treated solutions, respectively, and the concentration was taken to be proportional to the absorbance at the analytical wavelength (Beer-Lambert law).

3. Results and Discussion

$BaTiO_3$ and $Ba_{0.97}Sr_{0.03}TiO_3$ powders were obtained by the co-precipitation method and sintered at 900 °C and 1000 °C for 4 hours. The effect of Sr substitution on the structure, functional groups, particle-size distribution, and photocatalytic activity was examined using 10 ppm MB solution as a model pollutant. XRD was used to determine the crystal structure and FTIR to identify the functional groups. UV-Vis spectrophotometry was used to follow the MB concentration during the photocatalytic test, and PSA was used to determine the particle-size distribution.

3.1. Crystal structure and Crystallite Size

The XRD patterns are shown in Figure 2, and the phases were identified using ICDD card No. 83-1880 for $BaTiO_3$. All samples show the main perovskite reflections, (100) to (311), at positions close to the reference pattern. The (101) reflection of the Sr-containing samples appeared at 31.567° (900 °C) and 31.585° (1000 °C), compared with 31.555° and 31.584° for undoped $BaTiO_3$ (inset of Figure 2), i.e., shifts of +0.012° and +0.001°, which are smaller than the step size of the scan (0.024°) and therefore not resolved.

Because Sr^{2+} (1.44 Å) is smaller than Ba^{2+} (1.61 Å), partial substitution at the A-site is expected to reduce the unit-cell volume and shift the reflections toward higher angles [27,28]. The present data are consistent with this direction but too small to demonstrate Sr incorporation, which would require compositional analysis (e.g., EDX, XRF, or ICP). Weak reflections that do not belong to $BaTiO_3$ are visible in all patterns (Figure 2). Those at about 23.9° and 28.8° coincide with the two strongest lines of barium oxalate, BaC_2O_4 (ICDD 19-0125; 23.90° and 28.78°), and are much more intense in the Sr-containing samples (the 28.8° peak is about 4-8 times higher than in undoped $BaTiO_3$). The assignment is tentative because other lines of this card (e.g., 18.4° and 19.5°) are weak or not resolved, and the persistence of oxalate after sintering at 900-1000 °C is chemically unexpected. Further weak reflections at about 25.1°, 27.5°, 29.3°, 34.6°, 36.2°, and 41.5° were not assigned. The larger amount of secondary phases in the Sr-containing samples suggests that part of the added precursors did not enter the perovskite lattice, so the Sr content of the perovskite phase may be lower than the nominal 3 mol%. Nevertheless, all samples retain the perovskite framework.

Copyright © 2027, ISSN 1978-2993

Table 2 and Table 3 summarize the crystallite size, crystallinity, and lattice parameters. The (002) and (200) reflections near 45° are resolved as a doublet at about 45.0° and 45.3-45.4° in all samples (Figure 2), and the splitting is clearer at 1000 °C. This identifies the perovskite phase of both $BaTiO_3$ and $Ba_{0.97}Sr_{0.03}TiO_3$ as tetragonal (P4mm), and no separate cubic reflections were identified. The lattice parameters in Table 3 give c > a, with c/a = 1.006 (0% Sr) and 1.006 (3% Sr) at 900 °C, and 1.008 and 1.007 at 1000 °C. Thus, the tetragonality of undoped $BaTiO_3$ increased with sintering temperature, and Sr substitution decreased c/a slightly at both temperatures. The unit-cell volumes calculated from Table 3 are 64.27 and 64.22 Å^3 at 900 °C and 64.13 and 64.1 Å^3 at 1000 °C for 0% and 3% Sr, respectively. The decrease of 0.03-0.05 Å^3 caused by Sr is in the expected direction but smaller than the uncertainty of the estimate (about ±0.1 Å^3), so it does not by itself confirm Sr incorporation.

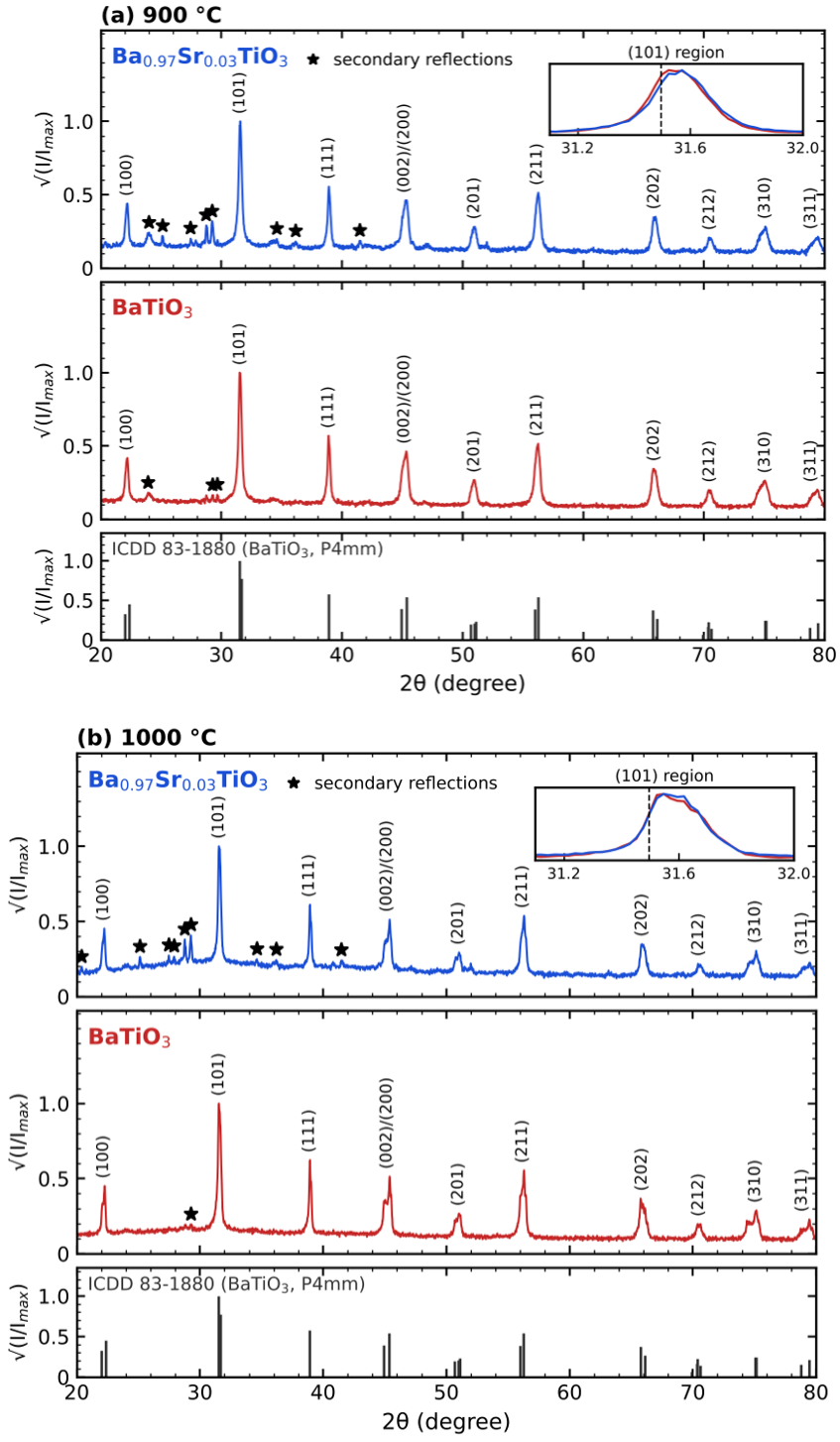


Figure 2. XRD patterns of $BaTiO_3$ and $Ba_{0.97}Sr_{0.03}TiO_3$ sintered at (a) 900 °C and (b) 1000 °C.

Copyright © 2027, ISSN 1978-2993

Table 2 gives crystallite sizes of 31.05 nm and 29.62 nm for $BaTiO_3$, and 32.66 nm and 32.22 nm for $Ba_{0.97}Sr_{0.03}TiO_3$, at 900 °C and 1000 °C, respectively, i.e., a slight decrease with sintering temperature, contrary to the usual expectation. These values are the intercepts of linear fits of ln β versus ln (1/cos θ) over ten reflections, but the fits are poor: R^2 = 0.17-0.62, and the slopes (1.7-3.4) deviate strongly from the value of 1 expected when the broadening is caused by crystallite size alone. The broadening is therefore not purely size-related. The tetragonal doublets, such as (002)/(200) near 45°, whose splitting is more pronounced at 1000 °C (Table 3), inflate the apparent FWHM, and microstrain and the absence of an instrumental-broadening correction add to this. The sizes in Table 2 should consequently be regarded as rough estimates. The (111) reflection near 38.9°, which is not split in the tetragonal phase, gives sizes of 36.5 nm (0% Sr) and 39.4 nm (3% Sr) at 900 °C and 45.7 nm and 42.0 nm at 1000 °C, i.e., an increase with sintering temperature, as expected, and no consistent effect of Sr (larger at 900 °C, smaller at 1000 °C). The crystallinity index in Table 2 differs by less than 1.5 points among the samples (96.27%, 95.28%, 94.81%, and 95.00%). It reflects the ratio of peak to background intensity rather than the crystalline fraction, so these small differences are not interpreted. Crystallite size refers to the coherent diffraction domain obtained from XRD, whereas particle size refers to the size of particles or agglomerates measured by DLS.

3.2. Optical Properties

The UV-Vis spectra in Figure 3 refer to the MB solution and not to the catalyst powders. No diffuse-reflectance (DRS) measurement or band-gap value of the catalysts is therefore reported here, and the electronic effect of Sr substitution is not discussed quantitatively. $BaTiO_3$ is a wide-band-gap semiconductor that absorbs mainly in the UV region, which is consistent with the use of UV irradiation in this study.

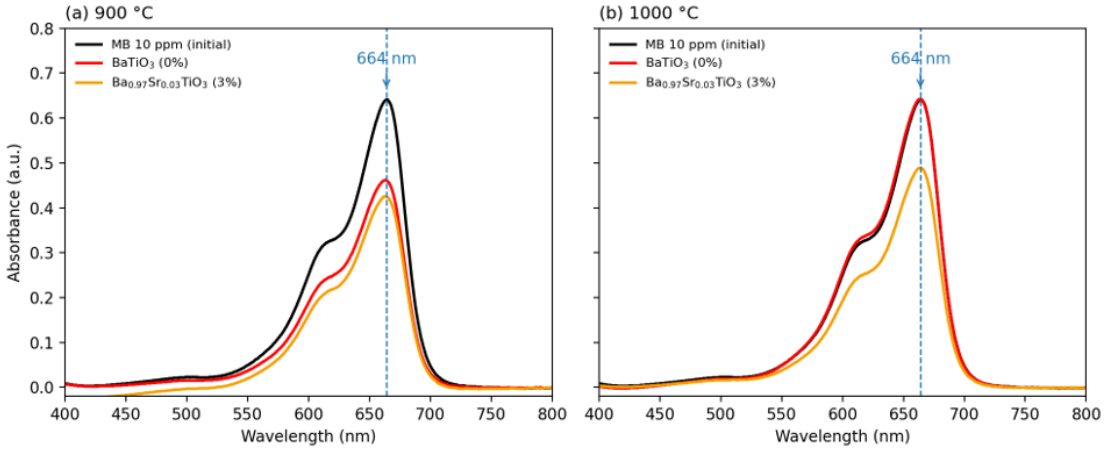


Figure 3. UV-Vis absorption spectra of the initial 10 ppm MB solution and of the solutions after photocatalytic treatment with $BaTiO_3$ (0%) and $Ba_{0.97}Sr_{0.03}TiO_3$ (3%) sintered at (a) 900 °C and (b) 1000 °C. The spectra were baseline-corrected by subtracting the absorbance at 800 nm.

Table 2. Crystallite size (nm) and crystallinity index (%) of $BaTiO_3$ and $Ba_{0.97}Sr_{0.03}TiO_3$ (Scherrer-plot method, ten reflections, no instrumental correction).

Mol Concentration	Crystallite Size (nm)		Crystallinity (%)	
	900 °C	1000 °C	900 °C	1000 °C
Sr = 0%	31.05	29.62	96.27	94.81
Sr = 3%	32.66	32.22	95.28	95.00

Table 3. Lattice parameters of the tetragonal phase of $BaTiO_3$ and $Ba_{0.97}Sr_{0.03}TiO_3$, estimated from the (002) and (200) reflections (uncertainty about ±0.003 Å).

Mol Concentration	Lattice Parameter			
	900 °C		1000 °C	
	a=b (Å)	*c (Å)*	*a=b (Å)*	*c (Å)*
Sr = 0%	3.997	4.022	3.992	4.024
Sr = 3%	3.997	4.020	3.993	4.021

Copyright © 2027, ISSN 1978-2993

3.3. Photocatalytic Activity

The photocatalytic activity was evaluated by the degradation of 10 ppm MB under UV irradiation. Figure 3 shows the absorbance spectra of the initial MB solution and of the solutions after treatment with $BaTiO_3$ (0%) and $Ba_{0.97}Sr_{0.03}TiO_3$ (3%). Figure 3 shows that MB has its main absorption peak at 664 nm, with a shoulder at about 620 nm, in agreement with the values usually reported for MB in dilute aqueous solution; 664 nm was therefore used for quantification. After treatment, the baseline-corrected absorbance at 664 nm decreased from 0.641 for the initial MB solution to 0.462 ($BaTiO_3$) and 0.425 ($Ba_{0.97}Sr_{0.03}TiO_3$) for the powders sintered at 900 °C, and to 0.642 ($BaTiO_3$) and 0.489 ($Ba_{0.97}Sr_{0.03}TiO_3$) for those sintered at 1000 °C. Assuming proportionality between absorbance and concentration, these values correspond to an apparent MB removal of about 28% ($BaTiO_3$) and 34% ($Ba_{0.97}Sr_{0.03}TiO_3$) at 900 °C, and about 0% and 24% at 1000 °C (Table 4). The Sr-containing powder therefore gave a larger apparent removal than undoped $BaTiO_3$ at both temperatures, and the higher sintering temperature decreased the apparent removal of both compositions. $BaTiO_3$ sintered at 1000 °C showed no measurable change in absorbance relative to the initial solution (0.642 versus 0.641), and its spectrum practically overlaps that of the initial MB solution in Figure 3b.

Although aliquots were taken at 15-minute intervals during the test, only one spectrum per sample is available for analysis here, so the reaction kinetics were not evaluated. Each value comes from a single spectrum without replicate measurements, so small differences (e.g., 28% versus 34% at 900 °C) are within the likely experimental uncertainty and are tentative, whereas the near-zero removal of $BaTiO_3$ at 1000 °C and the decrease with sintering temperature are larger. The spectrum of $Ba_{0.97}Sr_{0.03}TiO_3$ sintered at 900 °C was recorded with a coarser wavelength step (2 nm) and had a negative baseline; without baseline correction its apparent removal would be 38% instead of 34%. The suspensions were stirred in the dark for 30 minutes before irradiation, which accounts for part of the adsorption, but the absorbance after the dark stage and a catalyst-free (photolysis) blank are not reported here. The decrease in absorbance therefore cannot be assigned exclusively to photocatalytic degradation, as residual adsorption on the powder surface and direct photolysis may contribute, and the values in Table 4 are reported as apparent removal.

The larger apparent removal of $Ba_{0.97}Sr_{0.03}TiO_3$, and the decrease for both compositions after sintering at 1000 °C, may be related to several factors. The crystallite size from the (111) reflection increased with sintering temperature (Section 3.1), which would be consistent with a lower surface area and fewer active sites at 1000 °C, although the surface area was not measured. Other possibilities are differences in tetragonality (Table 3), in the amount of secondary phases (Figure 2), in MB adsorption, or reduced electron-hole recombination. The agglomerate size from DLS does not follow the same trend (Table 5; for example, the 1000 °C samples have the same Z-average but very different removal), so no single cause can be assigned. None of these possibilities was examined directly in this study; reduced recombination and improved charge separation in particular are hypotheses only, and verifying them would require photoluminescence spectroscopy, photocurrent measurements, electrochemical impedance spectroscopy, or time-resolved spectroscopy. Accordingly, the mechanism is not concluded here.

Table 4. Apparent MB removal calculated from the absorbance at 664 nm (Figure 3). A_0 = 0.644 (raw) and 0.641 (baseline-corrected).

Sample	Sintering (°C)	A (664 nm), raw	A (664 nm), corrected	Apparent removal (%)
$BaTiO_3$ (Sr = 0%)	900	0.464	0.462	28
$Ba_{0.97}Sr_{0.03}TiO_3$ (Sr = 3%)	900	0.399	0.425	34
$BaTiO_3$ (Sr = 0%)	1000	0.645	0.642	≈ 0
$Ba_{0.97}Sr_{0.03}TiO_3$ (Sr = 3%)	1000	0.503	0.489	24

Table 5. DLS results (mean ± standard deviation of three runs).

Sample	Sintering (°C)	Z-average (nm)	PDI	Intensity peak (nm)
$BaTiO_3$ (Sr = 0%)	900	441.8 ± 2.9	0.36 ± 0.04	472 ± 21
$Ba_{0.97}Sr_{0.03}TiO_3$ (Sr = 3%)	900	256.6 ± 8.8	0.28 ± 0.03	260 ± 10
$BaTiO_3$ (Sr = 0%)	1000	371.2 ± 16.6	0.33 ± 0.04	382 ± 46
$Ba_{0.97}Sr_{0.03}TiO_3$ (Sr = 3%)	1000	373.8 ± 3.4	0.27 ± 0.02	393 ± 6

Copyright © 2027, ISSN 1978-2993

3.4. FTIR Analysis

Figure 4 summarizes the bonding scheme proposed for the synthesis route. In the Ti-oxalate complex, the carboxylate oxygen atoms of oxalate chelate Ti through covalent Ti-O bonds, and Ba^{2+} (and Sr^{2+}) is attached to the carboxylate groups mainly by ionic interaction. During sintering the oxalate groups are removed and the Ti-O-Ba(Sr) network of the perovskite is formed, in which Ti is octahedrally coordinated by six O atoms (TiO_6) and Ba/Sr occupies the A-site. This scheme is based on the general oxalate co-precipitation route, the observed Ti-O band, and the barium-oxalate-like reflections; the intermediate precursor was not isolated or characterized here, so the scheme is illustrative.

Figure 5 shows the FTIR spectra of the samples sintered at 900 °C and 1000 °C, plotted as transmittance versus wavenumber in the range of 350-4000 cm^{-1}. The O-H band indicates water adsorbed on the surface of the nanoparticles. Sr substitution decreased the intensity of the C-O vibrational peak and slightly changed the peak positions, but it did not change the type of functional groups in $BaTiO_3$. The strong absorption bands at 565.17-575.78 cm^{-1} are assigned to the Ti-O (Ba-Ti-O) stretching vibration of the perovskite lattice, which supports the formation of the $BaTiO_3$-type structure observed by XRD. The band at around 1432 cm^{-1} is associated with carbonate-related vibrations or residual organic compounds from the synthesis (possibly including remnants of the PVA binder), which is consistent with the secondary phase detected by XRD. A separate Sr-O band was not resolved, so FTIR alone does not confirm Sr incorporation.

3.5. Particle Size Distribution (PSA)

Figure 6 shows representative DLS size distributions weighted by intensity (for each sample, the run with the Z-average closest to the mean of the three runs), and Table 5 summarizes the Z-average hydrodynamic diameter, PDI, and intensity peak size from three repeated runs per sample. At 900 °C, the Z-average of $BaTiO_3$ was 441.8 ± 2.9 nm, whereas that of $Ba_{0.97}Sr_{0.03}TiO_3$ was 256.6 ± 8.8 nm, i.e., about 185 nm smaller. At 1000 °C, however, the two compositions gave the same Z-average within the run-to-run variation (371.2 ± 16.6 nm and 373.8 ± 3.4 nm). Raising the sintering temperature from 900 °C to 1000 °C decreased the Z-average of $BaTiO_3$ by about 70 nm but increased that of $Ba_{0.97}Sr_{0.03}TiO_3$ by about 117 nm. Thus, no consistent effect of Sr substitution or sintering temperature on the hydrodynamic size can be concluded: the smaller agglomerates of the Sr-containing powder were observed only at 900 °C. The PDI values (0.24-0.41) indicate moderately broad distributions and were slightly lower for the Sr-containing samples at both temperatures. All Z-average values (about 250-440 nm) are much larger than the crystallite size obtained from XRD (about 30-46 nm, Section 3.1), which indicates that the measured particles consist of many crystallites, i.e., they are agglomerates. The agglomeration may be caused by the high surface energy of nanoparticles and by particle coalescence at elevated sintering temperature. Because DLS reflects the state of dispersion (medium, concentration, sonication) as well as the powder itself, and only one synthesis batch per composition was measured, the opposite

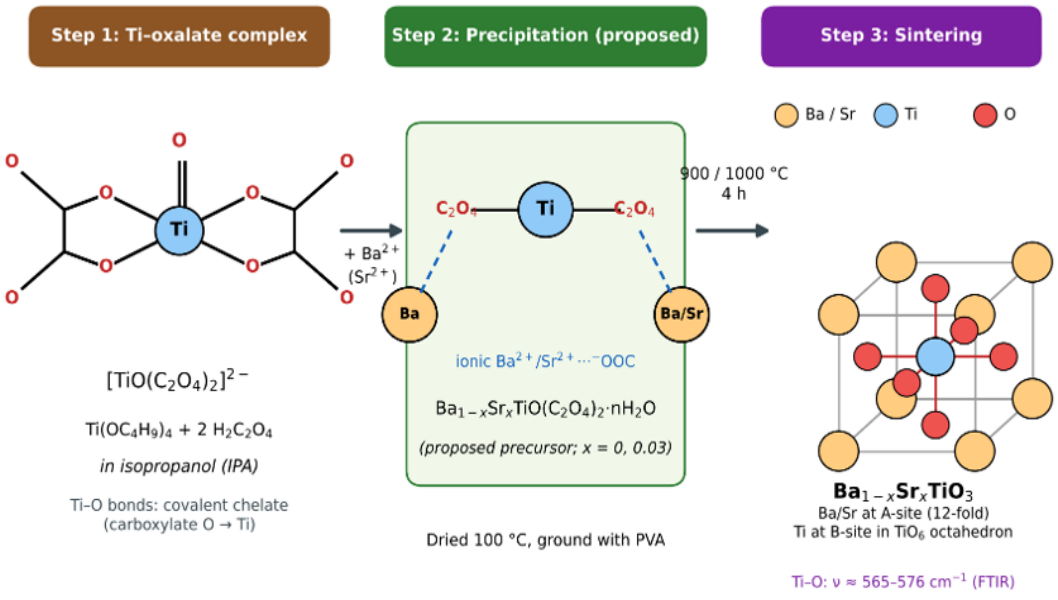


Figure 4. Proposed bonding scheme of the co-precipitation route: Ti-oxalate chelation, ionic attachment of Ba^{2+}/Sr^{2+}, and formation of the $Ba_{1-x}Sr_xTiO^3$ perovskite (TiO_6 octahedra, A-site Ba/Sr) after sintering.

Copyright © 2027, ISSN 1978-2993

temperature trends of the two compositions should not be interpreted as intrinsic effects without replicate batches. They might be related to differences in the strength of agglomerates formed during sintering, but this was not tested, and zeta potential was not measured. The intensity distributions also contain a small population at about 5000 nm (2-6% of the intensity), which accounts for 44-78% of the volume distribution. Because scattered intensity

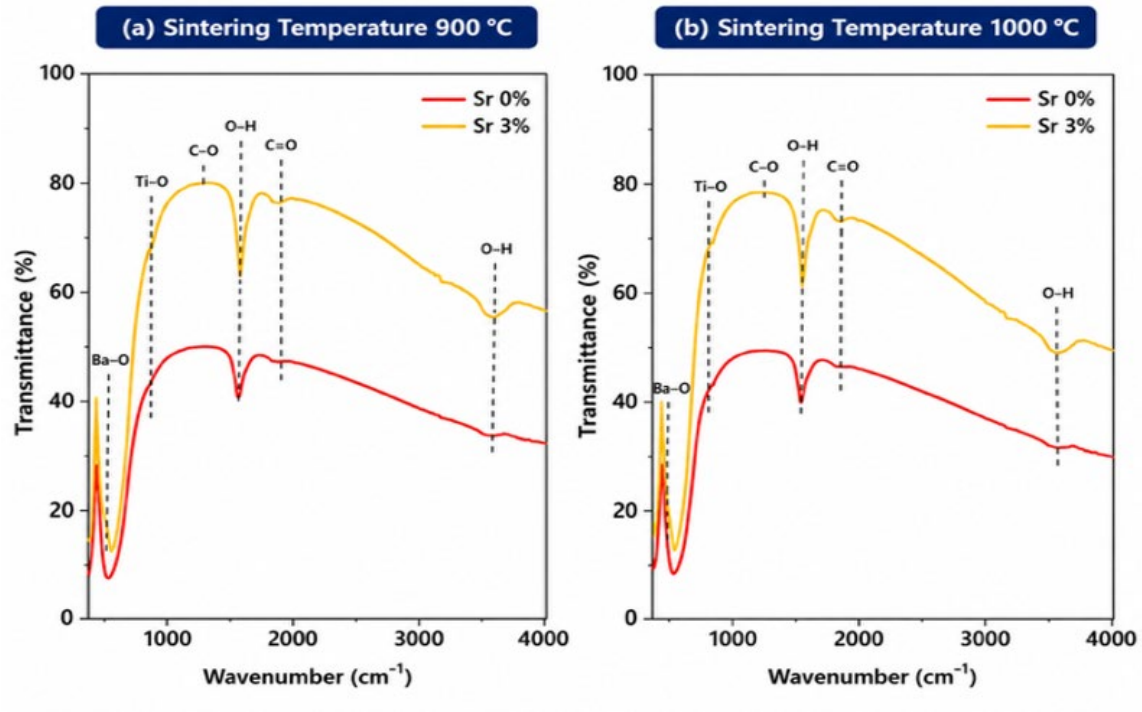


Figure 5. FTIR spectra of $BaTiO_3$ and $Ba_{0.97}Sr_{0.03}TiO_3$ sintered at 900 °C and 1000 °C.

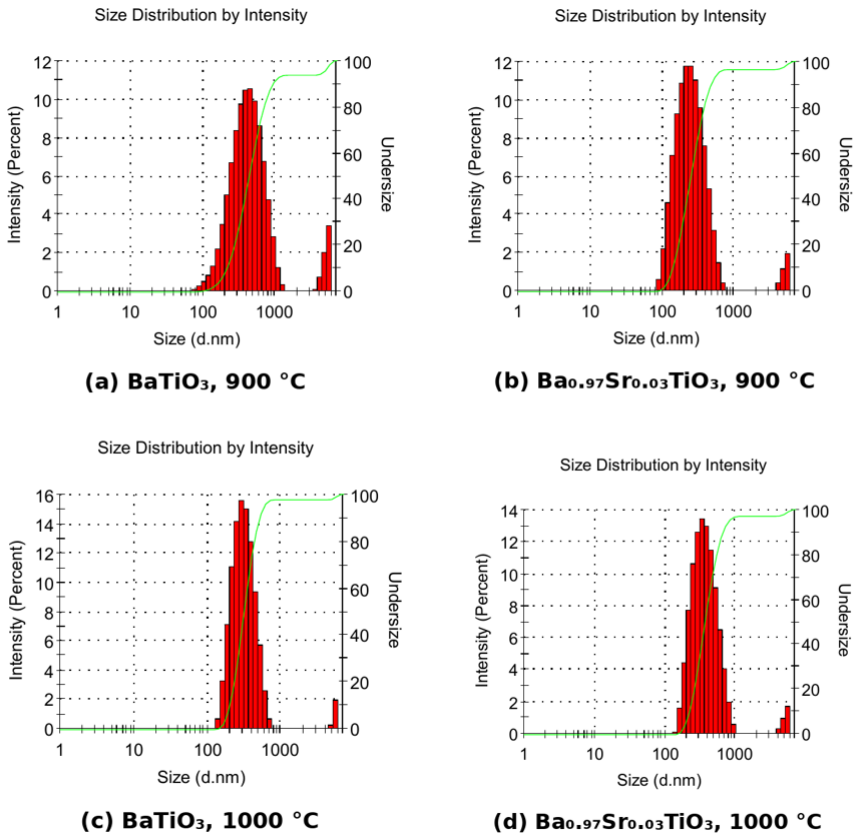


Figure 6. Representative DLS size distributions (by intensity) of (a) $BaTiO_3$ and (b) $Ba_{0.97}Sr_{0.03}TiO_3$ sintered at 900 °C, and (c) $BaTiO_3$ and (d) $Ba_{0.97}Sr_{0.03}TiO_3$ sintered at 1000 °C.

Copyright © 2027, ISSN 1978-2993

increases steeply with particle size, a few large aggregates or settling particles can dominate such distributions; therefore the volume and number distributions were not used for quantitative comparison. DLS measures the hydrodynamic diameter of particles and agglomerates in suspension and does not provide information on particle shape or microstructure; the morphology, primary particle size, and grain boundaries can only be confirmed by SEM or TEM observation, which was not performed in this study and is left for future work.

4. Conclusions

$BaTiO_3$ and $Ba_{0.97}Sr_{0.03}TiO_3$ nanomaterials were synthesized by the co-precipitation method and sintered at 900 °C and 1000 °C for 4 hours. XRD showed the tetragonal perovskite structure with weak secondary reflections, which were more numerous in the Sr-containing samples, and no resolved shift of the (101) reflection after 3 mol% Sr substitution, so Sr incorporation was not demonstrated by XRD alone. The crystallite size was about 30-33 nm from the Scherrer plot and 37-46 nm from the unsplit (111) reflection, which increased with sintering temperature, and DLS revealed agglomerates with Z-average diameters of about 250-440 nm; the Sr-containing powder was smaller only at 900 °C, and no consistent effect of sintering temperature was found. FTIR identified the characteristic Ti-O (Ba-Ti-O) stretching band of $BaTiO_3$. Under UV irradiation, the apparent MB removal (absorbance at 664 nm, single spectrum per sample) was higher for $Ba_{0.97}Sr_{0.03}TiO_3$ (about 34% and 24% at 900 °C and 1000 °C) than for undoped $BaTiO_3$ (about 28% and 0%), and the higher sintering temperature decreased the apparent removal of both compositions. The mechanism was not established; band-gap analysis, adsorption and photolysis controls, kinetic analysis, and charge-carrier characterization are needed in future work.

Acknowledgements

The authors would like to thank DRTPM, Ministry of Education, Culture, Research, and Technology of Indonesia, for funding this research under the 2022 Beginner Lecturer Research (PDP) scheme, with support from LLDIKTI Region VI and LPPM, under Contract Nos. 158/E5/PG.02.00.PT/2022, 042/LL6/PB/AK.04/2022, and 02.06/PL2/LPPM/2022.

Conflict of Interest

The authors declare no conflict of interest.

Declaration of Generative AI Use

During the preparation of this manuscript, AI-assisted tools were used only for language improvement and grammar correction. The authors carefully reviewed and edited the manuscript and take full responsibility for the content of the publication.

CRediT Author Statement

Author Contributions: Elvinda Bendra Agustina conceived and carried out the research project, wrote the manuscript, and coordinated the collaboration among the authors. Abdul Hakim Prima Yuniarto, Trya Andini, and Alif Tiana Dewi contributed to the data collection and analysis. Yofentina Iriani assisted with the transcription of the data and critically revised the manuscript. All authors have read and agreed to the published version of the manuscript.

References

[1] Štrbac, D., Aggelopoulos, C.A., Štrbac, G., Dimitropoulos, M., Novaković, M., Ivetić, T., Yannopoulos, S.N. (2018). Photocatalytic degradation of naproxen and methylene blue: Comparison between ZnO, TiO_2 and their mixture. *Process Safety and Environmental Protection*, 113, 174-183. DOI: 10.1016/j.psep.2017.10.007

[2] Lin, J., Luo, Z., Liu, J., Li, P. (2018). Photocatalytic degradation of methylene blue in aqueous solution by using ZnO-SnO_2 nanocomposites. *Materials Science in Semiconductor Processing*, 87, 24-31. DOI: 10.1016/j.mssp.2018.07.003

[3] Isai, K.A., Shrivastava, V.S. (2019). Photocatalytic degradation of methylene blue using ZnO and 2%Fe–ZnO semiconductor nanomaterials synthesized by sol–gel method: a comparative study. *SN Applied Sciences*, 1, 1247. DOI: 10.1007/s42452-019-1279-5

[4] Xu, S., Guo, L., Sun, Q., Wang, Z.L. (2019). Piezotronic effect enhanced plasmonic photocatalysis by AuNPs/$BaTiO_3$ heterostructures. *Advanced Functional Materials*, 29, 1808737. DOI: 10.1002/adfm.201808737

[5] Fakhri-Mirzanagh, S., Ahadzadeh-Namin, K., Givi, G.P., Farazin, J., Azizian-Kalandaragh, Y. (2020). The effect of capping agent on the structural, optical properties and photocatalytic activity of MgO nanostructures. *Physica B: Condensed Matter*, 412064. DOI: 10.1016/j.physb.2020.412064

[6] Gao, Q., Xu, J., Bu, X.-H. (2019). Recent advances about metal–organic frameworks in the removal of pollutants from wastewater. *Coordination Chemistry Reviews*, 378, 17-31. DOI: 10.1016/j.ccr.2018.03.015

Copyright © 2027, ISSN 1978-2993

[7] Haruna, A., Abdulkadir, I., Idris, S.O. (2020). Effect of annealing temperature on the synthesis and photocatalytic properties of $Bi_{0.65}K_{0.2}Ba_{0.15}FeO_3$ perovskite-like nanoparticle synthesized by sol-gel method. *Beni-Suef University Journal of Basic and Applied Sciences*, 9, 1-8. DOI: 10.1186/s43088-020-0033-9

[8] Núñez-Salas, R.E., Hernández-Ramírez, A., Hinojosa-Reyes, L., Guzmán-Mar, J.L., Villanueva-Rodríguez, M., Maya-Treviño, M.d.L. (2019). Cyanide degradation in aqueous solution by heterogeneous photocatalysis using boron-doped zinc oxide. *Catalysis Today*, 328, 202-209. DOI: 10.1016/j.cattod.2018.11.061

[9] Betancourt-Buitrago, L.A., Hernandez-Ramirez, A., Colina-Marquez, J.A., Bustillo-Lecompte, C.F., Rehmann, L., Machuca-Martinez, F. (2019). Recent developments in the photocatalytic treatment of cyanide wastewater: An approach to remediation and recovery of metals. *Processes*, 7, 225. DOI: 10.3390/pr7040225

[10] Wang, Z.L., Wu, W., Falconi, C. (2018). Piezotronics and piezo-phototronics with third-generation semiconductors. *MRS Bulletin*, 43, 922-927. DOI: 10.1557/mrs.2018.263

[11] Pan, L., Sun, S., Chen, Y., Wang, P., Wang, J., Zhang, X., Zou, J.J., Wang, Z.L. (2020). Advances in piezo-phototronic effect enhanced photocatalysis and photoelectrocatalysis. *Advanced Energy Materials*, 10, 2000214. DOI: 10.1002/aenm.202000214

[12] Guo, Q., Zhou, C., Ma, Z., Yang, X. (2019). Fundamentals of TiO_2 photocatalysis: concepts, mechanisms, and challenges. *Advanced Materials*, 31, 1901997. DOI: 10.1002/adma.201901997

[13] Bie, C., Yu, H., Cheng, B., Ho, W., Fan, J., Yu, J. (2021). Design, fabrication, and mechanism of nitrogen-doped graphene-based photocatalyst. *Advanced Materials*, 33, 2003521. DOI: 10.1002/adma.202003521

[14] Qiu, X., Zhang, Y., Zhu, Y., Long, C., Su, L., Liu, S., Tang, Z. (2021). Applications of nanomaterials in asymmetric photocatalysis: recent progress, challenges, and opportunities. *Advanced Materials*, 33, 2001731. DOI: 10.1002/adma.202001731

[15] Chen, Y.H., Chen, Y.D. (2011). Kinetic study of Cu(II) adsorption on nanosized $BaTiO_3$ and $SrTiO_3$ photocatalysts. *Journal of Hazardous Materials*, 185, 168-173. DOI: 10.1016/j.jhazmat.2010.09.014

[16] Zheng, T., Wu, J., Xiao, D., Zhu, J. (2018). Recent development in lead-free perovskite piezoelectric bulk materials. *Progress in Materials Science*, 98, 552-624. DOI: 10.1016/j.pmatsci.2018.06.002

[17] Uchino, K. (2003). Piezoelectric ceramics. In Sōmiya, S. et al. (Eds.), Handbook of Advanced Ceramics. Elsevier, pp. 105-158.

[18] Fan, B., Yang, G., Li, M.-Y., Liu, P., Qiu, S., Shen, M., Liu, H., Zhang, G., Wang, Q., Jiang, S. (2018). Lead-free $Ba_{(1-x)}Sr_xTiO_3$ ceramics for room-temperature pyroelectric energy conversion. *Ceramics International*, 44, 8270-8276. DOI: 10.1016/j.ceramint.2018.02.009

[19] Boubaia, A., Assali, A., Berrah, S., Bennacer, H., Zerifi, I., Boukortt, A. (2021). Band gap and emission wavelength tuning of Sr-doped $BaTiO_3$ (BST) perovskites for high-efficiency visible-light emitters and solar cells. *Materials Science in Semiconductor Processing*, 130, 105837. DOI: 10.1016/j.mssp.2021.105837

[20] Hikmah, D.N., Sandi, D.K., Nurosyid, F., Iriani, Y. (2021). Effects of sintering temperature and holding times on the microstructure and chemical bond of strontium titanate ($SrTiO_3$). *Journal of Physics: Conference Series*, 2110, 012011. DOI: 10.1088/1742-6596/2110/1/012011

[21] Ali, A., Zaman, A., Aldulmani, S.A.A., Abbas, M., Mushtaq, M., Bashir, K., Amami, M., Althubeiti, K. (2022). Structural evolution and microwave dielectric properties of $Ba_{1-x}Sr_xTi_4O_9$ ($0.0 \leq x \leq 0.06$) ceramics. *ACS Omega*, 7, 2331-2336. DOI: 10.1021/acsomega.1c06212

[22] Coondoo, I., Krylov, A., Sharma, D.K., Krylova, S., Alikin, D., Kumar, J.S., Mirzorakhimov, A., Melnikova, N., Soares, M.J., Kholkin, A.L. (2022). Temperature dependent structural, dielectric, Raman, piezoresponse and photoluminescence investigations in sol-gel derived BCZT ceramics. *Materials Chemistry and Physics*, 277, 125526. DOI: 10.1016/j.matchemphys.2021.125526

[23] Sapkota, P., Fujii, I., Kim, S., Ueno, S., Moriyoshi, C., Kuroiwa, Y., Wada, S. (2022). Mn–Nb co-doping in barium titanate ceramics by different solid-state reaction routes for temperature stable and DC-bias free dielectrics. *Ceramics International*, 48, 2154-2160. DOI: 10.1016/j.ceramint.2021.09.304

[24] Iriani, Y., Nurosyid, F., Mayasari, R., Sandi, D.K. (2021). Annealing temperatures' effects on microstructure and optical properties of $Ba_{0.95}Sr_{0.05}TiO_3$ films. *Jurnal Sains Materi Indonesia*, 23, 31-36. DOI: 10.17146/jsmi.2021.23.1.6338

[25] Ulfa, U., Iriani, Y., Kusumandari, K. (2021). Microstructure, morphology, and dielectric properties of $Ba_{1-x}La_xTiO_3$ with variation mole concentration of lanthanum by co-precipitation method. *IOP Conference Series: Materials Science and Engineering*, 1096, 012138. DOI: 10.1088/1757-899X/1096/1/012138

[26] Chen, X., Chao, X., Yang, Z. (2019). Submicron barium calcium zirconium titanate ceramic for energy storage synthesised via the co-precipitation method. *Materials Research Bulletin*, 111, 259-266. DOI: 10.1016/j.materresbull.2018.11.025

Copyright © 2027, ISSN 1978-2993

[27] Suchanicz, J., Sitko, D., Stanuch, K., Świerczek, K., Jagło, G., Kruk, A., Kluczewska-Chmielarz, K., Konieczny, K., Czaja, P., Aleksandrowicz, J., Wieczorek, W., Grygierek, J., Sokolowski, M., Stachowski, G., Antonova, M., Sternberg, A. (2023). Temperature and E-poling evolution of structural, vibrational, dielectric, and ferroelectric properties of $Ba_{1-x}Sr_xTiO_3$ ceramics (x = 0, 0.1, 0.2, 0.3, 0.4 and 0.45). *Materials*, 16, 6316. DOI: 10.3390/ma16186316

[28] Uddin, S., Hameed, S., Ali, N., Althubeiti, K., Zaman, A., Alrobei, H., Mushtaq, M., Ali, A., Sultana, F. (2021). Effect of Sr^{2+} doping on the phase transition of $BaTiO_3$ lead-free ferroelectric ceramics. *Materials Research Express*, 8, 096101. DOI: 10.1088/2053-1591/ac22c3.

Copyright © 2027, ISSN 1978-2993